Strategies to predict radiated sound fields from foldable, Miura-ori-based transducers for acoustic beamfolding

Danielle T. Lynd and Ryan L. Harne

Strategies to predict radiated sound fields from foldable, Miura-ori-based transducers for acoustic beamfolding

Danielle T. Lynd and Ryan L. Harne[a)]

Department of Mechanical and Aerospace Engineering, The Ohio State University, Columbus, Ohio 43210, USA

To bypass challenges of digital signal processing for acoustic beamforming applications, it is desirable to investigate repeatable mechanical approaches that accurately reposition transducers for real-time, simple guiding of acoustic energy. One promising approach is to create arrays configured on origami-inspired tessellated architectures. The low dimensionality, easy implementation, compactness, and use of straightforward folding to guide acoustic energies suggest that tessellated arrays may bypass limitations of conventional digital signal processing for beamforming. On the other hand, the challenge of developing such reconfigurable arrays lies in determining tessellation design and folding extent that direct sound as required. This research assesses the utility of the computationally efficient, approximate solutions to Rayleigh's integral to predict radiated sound fields from tessellated arrays based on Miura-ori fold patterns. Despite altering assumptions upon which the integral is derived, it is found that the salient beam-steering properties and amplitudes are accurately reconstructed by the analytical approach, when compared to boundary element model results. Within the far field angular space accommodated by the formulation assumptions, the analytical approach provides a powerful, time-efficient, and intuitive means to identify tessellated topologies and folding extents that empower desired wave-guiding functionalities, giving fuel to the concept of acoustic beamfolding. © 2017 Acoustical Society of America.
[http://dx.doi.org/10.1121/1.4974204]

I. INTRODUCTION

In propagative beamforming applications, active phase delays and amplitude weights are provided to spatially distributed and fixed transducers to virtually reposition the transducers such that radiated wavefronts constructively (destructively) interfere where energy must (must not) be delivered. This strategy is the basis for many communication, imaging, and hailing systems,[1,2] non-lethal force projection devices,[3,4] and sound field reproduction platforms.[5,6] By virtue of acoustic reciprocity, delaying and shading received signals from microphone array transducers achieves similarly large increases in acoustic wave directionality for applications of environmental imaging and measurement.[7–11] Yet, the digital signal processing methods that enable such beamforming with active phase delays introduce particular challenges associated with the computational cost, filter stability, complexity of implementation, and limited portability of the beamformer and signal processing system.[12–14] These difficulties are exacerbated when real-time beam steering is required, particularly for high frequencies.[15]

The alternative to computational methods to spatially resample or -distribute the transducers is to mechanically reposition the transducers within the array architecture.[38] Of course, mechanical methods are associated with no computational cost, although energy expense is accounted for via the means of repositioning, and stability is of little or no concern.

Mechanical methods of reconfiguration for arrays may also be developed to provide exceptional portability, straightforward implementation, and ease of tailoring performance in real-time, as will be clear through this report. Therefore, transducer arrays that leverage *mechanical signal processing* for focusing and steering wave energy have particular advantages over their digitally processed counterparts. "Frequency selective surfaces" for radio frequency antennae are prime examples where array shape change is leveraged for performance tuning that is more straightforward than a digital signal processing approach,[16–19] and astronomical observatories have long rearranged satellite receivers or transmitters to optimize long-range energy-guiding capability.[20]

On the other hand, similar to the open-endedness of developing digital methods to beam and guide sound energy, one has an infinite number of ways in which array transducers may be physically positioned and repositioned to steer sound, which may encumber system development and deployment. To drastically simplify the concerns of mechanical signal processing, this research investigates an innovative approach that bypasses such challenges and facilitates exceptional performance in real-time beamforming. The approach harnesses arrays of acoustic transducers configured along foldable, tessellated architectures inspired by origami patterns.[21] Origami, the ancient art of paper folding,[22] has recently provided diverse research fields with many inspirations for easy-to-fabricate and -deploy structures,[23,24] particularly those that exhibit significant topological changes according to a single degree-of-freedom of motion.[25–27]

a)Electronic mail: harne.3@osu.edu

Thus, exceptional multifunctionality is realized by first constructing the tessellation in the flat/unfolded state and then folding it into three-dimensional forms where it serves its several engineering purposes according to its instantaneous shape and associated properties.[28] For certain tessellations, the potential extends further because the architectures may be compacted in a fully folded state for easy transport.[29]

Taking all factors into account, the authors of this report recently introduced a new concept of acoustic beamfolding.[30] In this concept, arrays of acoustic transducers are configured and reconfigured along foldable, tessellated architectures to simply and significantly adapt sound energy-guiding capabilities using folding actions. Beamfolding represents the mechanical analogue to digitally processing signals to beam and steer acoustic energy. By using tessellated arrays that possess only one degree-of-freedom, the concept can be straightforward to leverage for high performance because considerable array shape change, and hence large change in array spectral directivity via the transducer repositioning, is achieved by folding. As a result, acoustic beamfolding bypasses the challenges of digital signal processing methods for steering acoustic energy and surmounts the inhibitions of mechanical signal processing by minimizing the open-endedness of design and deployment using tessellated architectures for large, global array reconfiguration with simple folding actions on one or a few degrees of freedom.[30] Thus, foldable, tessellated transducer arrays may find application wherever multi-purposing and/or portability of acoustic wave radiators are in demand. This may include enabling change in the energy beam of ultrasound probes by leveraging discrete and straightforward tessellated probe transducer surface reconfigurations or facilitating significant mobility for underwater towed arrays that are folded compact during transport and unfolded to different extents during deployment to mechanically steer beam patterns.

Yet, a concept of acoustic beamfolding also raises nontrivial questions regarding what tessellations are useful to greatly adapt sound energy-guiding performance by folding and how does one determine these capabilities in a strategic way to obtain generalized understanding of the full opportunities? Theoretical models would facilitate the discoveries needed to answer such questions at a fraction of time and/or cost associated with comparable investigations by computational or experimental methods alone. Although the authors introduced an analytical model for a tessellated acoustic array based on the Miura-ori fold pattern, wherein the Rayleigh's integral is approximately solved under different extents of folding,[30] the model was not utilized to address these broad, important questions whose answers could help firmly establish the beamfolding concept. Moreover, the model was verified only against a preliminary experimental dataset, and was derived via simplifications that may compromise its correctness. Thus, the value of a theoretical model built upon approximate solutions to Rayleigh's integral when applied to foldable, tessellated acoustic arrays remains to be conclusively determined.

Therefore, the objective of this research is to assess the suitability and effectiveness of employing an efficient analytical approach to predict the time-harmonic sound fields radiated from tessellated arrays configured along the Miura-

ori fold pattern. The Miura-ori tessellation has one kinematic degree of freedom and is an exemplary architecture to accommodate current manufacturing practices,[31,32] which makes it worthy of close consideration as an architecture intended for beaming sound by folding actions. The boundary element method (BEM) is employed as a counterpart modeling approach for verification purposes. This report is organized as follows. Section II overviews the tessellated geometry of interest and the method undertaken to predict the sound pressure level (SPL), delivered from the array to the field, via approximate solutions to Rayleigh's integral. Considerable enhancements are made to the original derivation to maximize its correctness and effectiveness for sound field prediction. Then, a critical assessment of the analytical modeling approach is conducted to characterize the broad utility of an efficient, simple means to predict sound directionality properties of tessellated and transducers.

II. ANALYTICAL MODEL REVIEW AND ENHANCEMENT

The unit cell of the Miura-ori fold pattern is shown in Fig. 1. It consists of four parallelogram facets defined by edge lengths a and b and an edge angle γ. When folded with dihedral fold angle θ, the unit cell raises from the x–y plane with a height of H at the peak. For brevity, the geometric relations among the folded unit cell extents S, L, V, and H with the edge lengths and edge and fold angles are not repeated here, but are provided in Ref. 30. The idea leveraged in the concept of acoustic beamfolding is that each parallelogram of the unit cell is a planar radiator, for instance, driven by discrete piezoelectric discs, Fig. 1 top right inset, or continuously distributed piezoelectric films.[30] The Miura-ori unit cell is defined by one kinematic degree of freedom, the fold angle $\theta \in [0, \pi/2]$ rad. Transitions in θ take the cell from an unfolded state $\theta = 0$ with zero unit cell volume, to a flat-
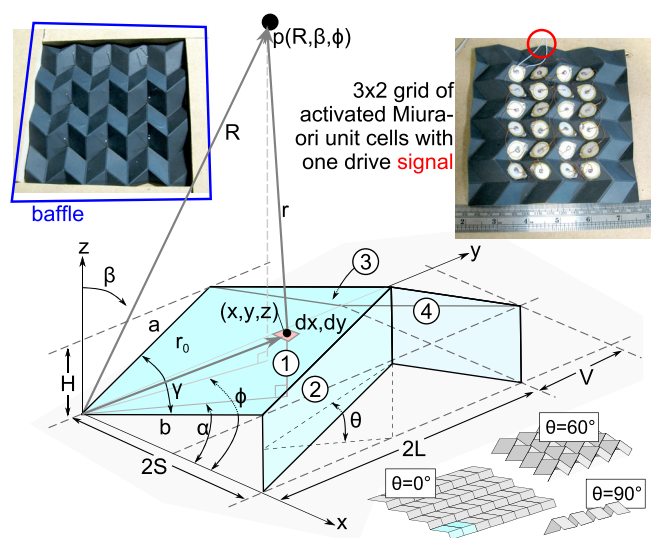

FIG. 1. (Color online) Geometry of Miura-ori unit cell and point in acoustic field. Insets, clockwise from top left, are a photograph of a fabricated tessellated array in a baffle for experimentation, photographs of piezoelectric drivers on the array underside with one drive signal required for operation, and an illustration of folding influence upon the array geometry.

foldable (compacted) state $\theta = \pi/2$ rad also with zero volume. Thus, assembling many of these unit cells together facilitates significant shape change due to a shared degree of freedom among the cells, Fig. 1 bottom right inset. From the standpoint of acoustics, the considerable sensitivities of an acoustic array relating to the spatial distribution and orientation of each array transducer[12] suggests that an array configured according to a tessellated pattern like Miura-ori would empower significant adaptation of beam steering performance by the acts of folding. Since the directionality of acoustic wave propagation is tuned by folding rather than electronically, the concept requires only one drive signal for all transducer elements, top right inset of Fig. 1, which considerably simplifies real-time implementation and manufacture. It is therefore needed to model this architecture to elucidate the opportunities. In the following paragraphs, the analytical model introduced in Ref. 30 is reviewed and built upon in new ways.

Rayleigh's integral[33] is the means by which to determine the acoustic pressure induced by a source distributed in space at a field point not coincident with the source. For finite-sized planar radiators, by virtue of practical utilization, it is a common convention to assume the radiator is baffled in an infinite, rigid plane.[34] This effectively bounds the spatial Fourier transform of the Rayleigh's integral to the region associated with non-zero radiator oscillation and modifies the pressure amplitude delivered to the field point depending on source geometry. Likewise, here the model formulation considers that the radiating tessellations are baffled, both individually and along the array perimeter. It is apparent that the assumptions regarding baffling are altered with respect to convention, since a rigid infinite plane clearly does not baffle each parallelogram source. Yet, as will be shown in this report, for a wide range of folding extents of the tessellated array, implementing Rayleigh's integral in this way facilitates a valuable degree of accuracy in the resulting predictions of radiated sound directionality and amplitude.

In applications of acoustic transducer development, the Rayleigh's integral is often applied over surfaces in the plane $z = 0$ (Ref. 35), although its derivation is applicable to distributions of point sources situated arbitrarily within a volume.[33] In the current case, the two approaches are integrated because the planar tessellated transducers do not rest in $z = 0$, unless the array is unfolded $\theta = 0$, and indeed they rotate and translate from $z = 0$ as $0 < \theta \le 90°$. Considering the schematic of Fig. 1, the Rayleigh's integral for the unit cell is

$$p_{cell}(R, \beta, \phi, t) = j\frac{\rho_0 \omega u_0}{2\pi} e^{j\omega t} \int_A \frac{e^{-jkr}}{r} \, dA, \quad (1)$$

where $\rho_0 = 1.104 \, \text{kg m}^{-3}$ is the air density; ω is the angular frequency of oscillation of the surface; u_0 is the spatially uniform, normal, velocity amplitude of the structure-fluid interfacing surface; A is the surface area of the array; $k = \omega/c$ is the acoustic wavenumber, with $c = 340 \, \text{m s}^{-1}$ as the sound speed; r is the distance from an oscillating differential area element dA to the far field pressure point $p(R, \beta, \phi, t)$ that is a distance R from the origin and positioned according to angles β in elevation and ϕ in azimuth.

Considering the geometry shown in the schematic of Fig. 1, the far field distance between the differential source element of area dA at (x, y, z) and the field point at (R, β, θ) is $r = R - r_0 \sin \beta \cos [\phi - \alpha] - z \cos \beta$. Based on an argument regarding the uniform increase in height of the array via a given fold angle, which is an indicator of a single degree of freedom of motion, the authors in Ref. 30 did not account for the radiator surface height position that modifies the far field distance r by $-z \cos \theta$. The distance is included here for completeness, correctness, and, in fact, simplified model algorithm implementation. Substituting this far field relation into Eq. (1) for the complex exponential component, and $r = R$ for the denominator component, one obtains

$$p_{cell}(R, \beta, \phi, t) = j\frac{\rho_0 \omega u_0}{2\pi} e^{j\omega t} \frac{e^{-jkR}}{R} \int_A e^{j(\Psi_1 x + \Psi_2 y + \Psi_3 z)} \, dx \, dy \quad (2)$$

where $\Psi_1 = k \sin \beta \cos \phi$, $\Psi_2 = k \sin \beta \sin \phi$, and $\Psi_3 = k \cos \theta$. To evaluate the integral, the area A must be defined. The surfaces of the parallelograms, numbered 1–4 in Fig. 1, are, respectively, defined by the geometry

$$x_1 \in [0, S]; \quad y_{1,I}(x) = \frac{V}{S}x; \quad y_{1,F}(x) = \frac{V}{S}x + L;$$

$$z_1 = \frac{H}{LS}(-Vx + Sy), \quad (3)$$

$$x_2 \in [S, 2S]; \quad y_{2,I}(x) = -\frac{V}{S}x + 2V;$$

$$y_{2,F}(x) = -\frac{V}{S}x + L + 2V;$$

$$z_2 = \frac{H}{LS}(Vx + Sy) - 2V\frac{H}{L}, \quad (4)$$

$$x_3 \in [0, S]; \quad y_{3,I}(x) = \frac{V}{S}x + L; \quad y_{3,F}(x) = \frac{V}{S}x + 2L;$$

$$z_3 = \frac{H}{LS}(Vx - Sy) + 2H, \quad (5)$$

$$x_4 \in [S, 2S]; \quad y_{4,I}(x) = -\frac{V}{S}x + L + 2V;$$

$$y_{4,F}(x) = -\frac{V}{S}x + 2L + 2V;$$

$$z_4 = \frac{H}{LS}(-Vx - Sy) + 2V\frac{H}{L} + 2H. \quad (6)$$

The subscripts on y in Eqs. (3)–(6) denote I initial and F final limits of integration to be used in Eq. (7). It is noted that the relations (3)–(6) are considerably different than those in Ref. 30, which is the result of explicitly accounting for the height z of the differential radiator surface element dA. Then, the integral form of Eq. (2) is decomposed into a summation of integral components, one for each radiator

$$p_{cell}(R, \beta, \phi, t) = j\frac{\rho_0 \omega u_0}{2\pi} e^{j\omega t} \frac{e^{-jkR}}{R}$$

$$\times \left\{ \sum_{i=1}^{4} \int_{x_i} \int_{y_i} e^{j(\Psi_1 x + \Psi_2 y + \Psi_3 z_i)} \, dy \, dx \right\}. \quad (7)$$

Danielle T. Lynd and Ryan L. Harne

RIGHTS LINK

By expressing the location of the differential area explicitly according to the plane geometries z_i, there is no need to accommodate a rotation of the plane via modified Ψ_i expressions for each parallelogram, which is the remedial strategy used by the authors in Ref. 30, since Eq. (7) is correct without need for amendment. This is a significant improvement to the analytical model fidelity and simplification in its implementation compared with the prior derivation established in Ref. 30. For later use, the unit cell beam pattern is distinguished in Eq. (7) by curly brackets { } and is denoted $h_{\mathrm{cell}}(\beta, \phi)$.

The product theorem[36] is employed to account for two-dimensional array assembly of directional transducers, where M_x and M_y numbers of unit cell transducer sets are configured in the x and y axes, respectively, according to the tessellation pattern. The array beam pattern for the tessellation is

$$h(\beta, \phi) = \frac{\sin[M_x kS \sin\beta\cos\phi]}{M_x \sin[kS \sin\beta\cos\phi]} \frac{\sin[M_y kL \sin\beta\sin\phi]}{M_y \sin[kL \sin\beta\sin\phi]}.$$
(8)

Consequently, the sound pressure delivered to the field point is

$$
\begin{aligned}
p(R, \beta, \phi, t) &= j\frac{\rho_0 \omega u_0}{2\pi} M_x M_y e^{j\omega t} \frac{e^{-jkR}}{R} h(\beta, \phi) \\
&\quad \times \sum_{i=1}^{4} \int_{x_i}\int_{y_i} e^{j(\Psi_1 x + \Psi_2 y + \Psi_3 z_i)}\, dy\, dx \\
&= j\frac{\rho_0 \omega u_0}{2\pi} M_x M_y e^{j\omega t} \frac{e^{-jkR}}{R} h(\beta, \phi) h_{\mathrm{cell}}(\beta, \phi).
\end{aligned}
$$
(9)

Because of the folding actions, Eq. (9) is not viable for predictive purposes across the elevation angles $\beta > \pi/2 - \theta$ or $\beta < -\pi/2 + \theta$ where a direct line-of-sight path from the transducer to the field point is unavailable for at least one of the tessellated surfaces. Thus, analytical predictions presented here omit results corresponding to these conditions. Finally, the SPL, with reference pressure $p_{\mathrm{ref}} = 20\,\mu\mathrm{Pa}$, is

$$\mathrm{SPL} = 20\,\log_{10}\left[\frac{p_{\mathrm{rms}}(R, \beta, \phi, t)}{p_{\mathrm{ref}}}\right],$$
(10)

where the subscript "rms" denotes the root-mean-square value.

III. RESULTS AND DISCUSSIONS

In Secs. III A, III B, and III C, the analytical model, developed upon approximate solutions to Rayleigh's integral is assessed with respect to high fidelity simulations conducted using the BEM, and implemented in the openBEM code architecture[37] in MATLAB. All computations are conducted on a computer outfitted with an Intel Core i7-4790 processor (Santa Clara, CA) and 32 GB of memory. As shown in Fig. 2(a), the boundary element mesh is closed around the activated area (which is the area exhibiting harmonic velocity

normal to the surface to propagate waves). Namely, at the edges of the array is a perimeter of the tessellation pattern that is not activated, identical to the experimental approach shown in the top right inset of Fig. 1. This strategy prevents edge radiation phenomena that would be in discord with the analytical model assumption and more closely "baffles" the activated transducers at the periphery of the array via the smooth transition to non-activated elements. In addition, the perimeter is itself baffled: in the case of the BEM model, the perimeter is extended to create an effective loudspeaker cabinet, while the experimental method is to enclose the perimeter in medium-density fiberboard (top left inset of Fig. 1). In all cases reported here, $a = 23\,\mathrm{mm}$, $b = 20.9\,\mathrm{mm}$, and $u_0 = 10\,\mathrm{mm/s}$. Also, $R = 7.17\,\mathrm{m}$ is selected so as to consider a field point sufficiently within the far field of the tessellated array; this distance is many times greater than the near-to-far field transition distance for the array dimensions and acoustic wavelengths under consideration. The BEM models utilize a minimum of 7.22 elements per acoustic wavelength to ensure accurate results are obtained.[34] Using such standards as those described above, the BEM model results serve as the benchmark against which predictions from the analytical model, greatly enhanced here, are to be evaluated.

A. Preliminary assessment and computational comparison

Figures 2(b) and 2(c) present the BEM model and analytical model results of SPL, respectively, for an array of the transducers with $\gamma = 45°$ along a tessellated folding pattern extending by $M_x = 4$ and $M_y = 4$, termed the 4×4 array, when it is mostly unfolded, $\theta = 2°$, and driven at 4.5 kHz. The analytical predictions are clearly gratuitous in terms of the significance of destructive interference achieved in the pressure nodes, although the azimuthal and elevation locations of the pressure nodes and sidelobes are accurately reconstructed by the analysis when compared to the BEM results. The amplitude of the major lobe also deviates by less than 1 dB between the two modeling approaches. Considering the tessellated array once folded up to $\theta = 45°$, the predictions in Figs. 2(d) and 2(e), showing BEM and analytical results, respectively, reveal a couple of factors worth examining, despite the difficulty of comparing three-dimensional contours of SPL. First, the breadth of the major lobe is increased in elevation (particularly along $\phi = \pi/2$ rad) and the position of the first sidelobe increases by about 7 deg in elevation β (closer to the plane with the origin), which are characteristics reconstructed by both the computational and analytical models, although the analytical predictions are omitted beyond elevation angles conflicting with the constraint $\beta > \pi/2 - \theta$. Second, is an emphasis to the latter point: the analysis cannot usefully predict pressure wave propagation to field points influenced by acoustic shadows, diffraction, and so forth, since such phenomena are not accounted for in Rayleigh's integral.[33]

On the other hand, taking a view of a greater objective in beamforming applications, the analysis faithfully reconstructs the salient features of the major lobe, where acoustic energy is most directed for utilization, and reconstructs the
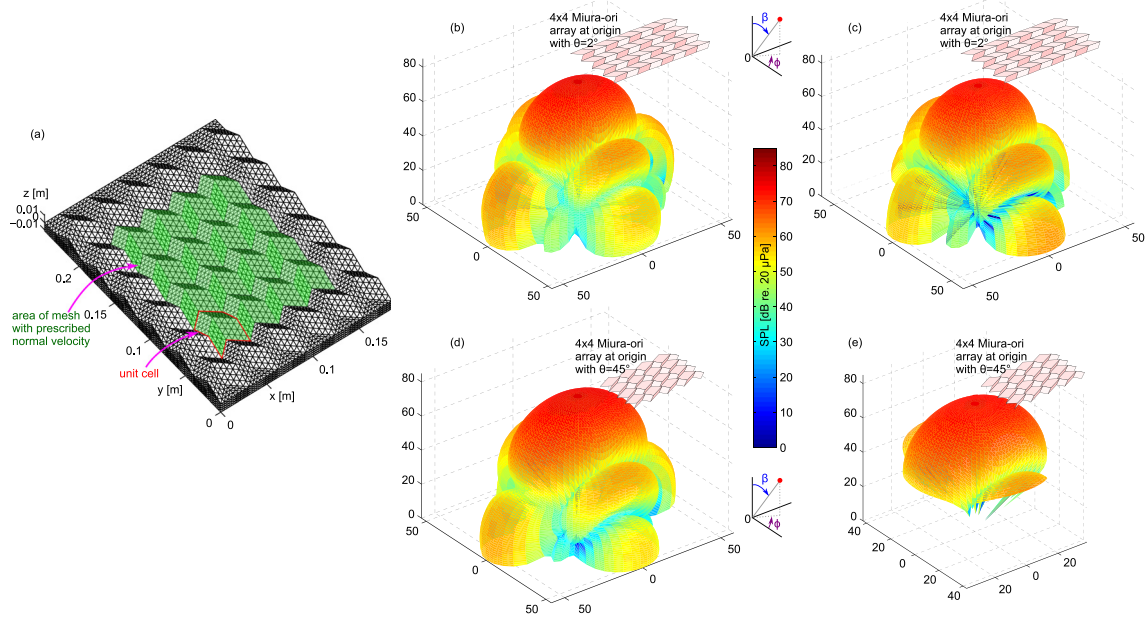
FIG. 2. (Color online) (a) BEM model mesh for a 4×4 tessellated array of transducers. (b) and (c) show the BEM and analytical models' predictions, respectively, for SPL in a spherical coordinate system when the array has a fold angle $\theta = 2°$ and is driven at 4.5 kHz]. (d) and (e) show the corresponding results, respectively, for fold angle $\theta = 45°$. In (b)–(e), all axes are in dB.

sidelobe and node characteristics. Adding to this the knowledge that the BEM computations for a single contour plot require ∼2200 s to complete (with four-core processing) while the analysis reconstructs the comparable contour in 28 ms (with single-core processing, and the time is not considerably influenced by the check of constraints to omit results). Thus, before discarding an approximate theoretical approach due to the inability to predict all characteristics of sound radiation even though it reconstructs the important features, one must carefully reflect on the computing speed increase of over 78 000 times that is facilitated by the analysis. In an early stage of system design and conceptualization, such expeditious modeling may serve a high value. Nevertheless, the confidence of utilizing the analytical tool must be bolstered through the close investigations that follow in Secs. III B and III C.

B. Assessment of SPL predictions with tessellated array

Figure 3 presents the SPL radiated from a 4×4 tessellated array with an edge angle $\gamma = 55°$, where the solid curves are BEM model results while the dashed curves are predictions generated by the analysis. The top (bottom) row corresponds to the SPL at 4.5 (7.0) kHz, and the columns from left to right present the SPL radiated for fold angles $\theta = 20, 40,$ and $60°$ with insets to illustrate the folding extents. The results are shown in four quadrants across the angles $\phi = [0, \pi/4, \pi/2, 3\pi/4]$ rad for four values of the azimuthal angle ϕ to provide an encompassing means for assessment at-a-glance. In Fig. 3 and in following similar figures, the results are omitted from presentation where the constraint on the viability of analytical predictions is violated, i.e., across $\beta > \pi/2 - \theta$.

For small fold angles $\theta = 20°$, Figs. 3(a) and 3(d), the two methods agree reasonably well regarding the various characteristics of the beamed sound, including the amplitude and breadth of the major lobe, the location of the pressure nodes according to the change in azimuth angle ϕ, and the relative SPL difference between the main and sidelobes. As the fold angle increases, both model compositions predict a broadening of the major lobe, while the sidelobes are modulated in elevation angle, number, and amplitude. It is evident that the analytical approach underpredicts the overall SPL as the fold angle increases to large values like $\theta = 60°$, Figs. 3(c) and 3(f). This is likely because the Rayleigh's integral accounts only for directly radiated sound (i.e., line-of-sight) while the BEM model may account for the lower frequency diffraction and reflection from adjacent transducer facets; evidence to support this claim is provided in Sec. III C. Yet, despite the discrepancy in overall SPL, the analysis effectively predicts the *relative* difference in SPL between the major lobe and sidelobes, as well as the sidelobe locations. All things considered, the comparison neither suggests perfection nor striking deficiency in the analytical approach. In fact, the findings indicate that the model is adequate if one's interest is to understand the capabilities of a foldable, tessellated array to an accuracy within a few degrees in space and several dB in most cases. From the perspective of assessing the effectiveness of the folded array to maintain a high proportion of sound energy constructively delivered to points at broadside, transducer and array efficiency measures may be considered.[1] These measures may include the ratio of radiated intensity in the major lobe after to the same intensity before folding, or, considering the analytical formulation, may be the intensity "lost" from the direct line-of-sight to the far field with respect to unfolded sound energy delivery. Indeed, efficiency measures for such foldable, tessellated
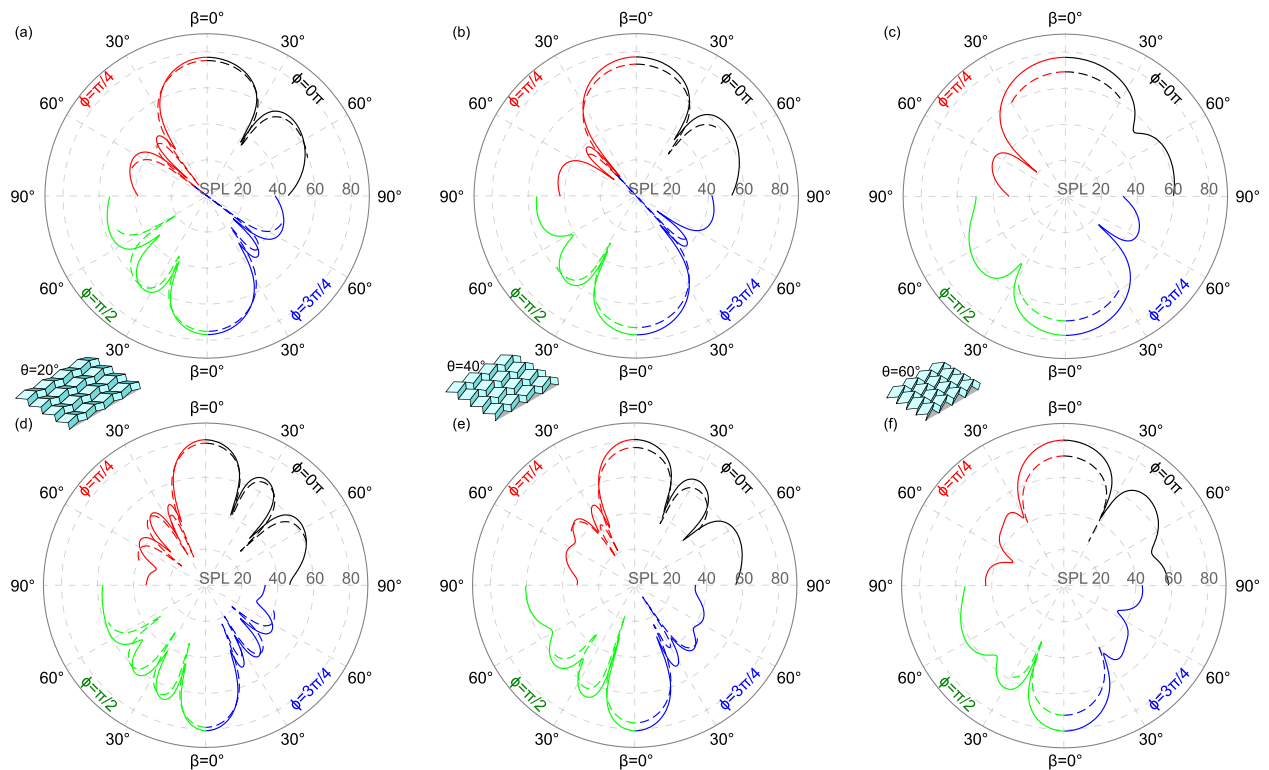
Danielle T. Lynd and Ryan L. Harne

FIG. 3. (Color online) SPL (dB re 20 μPa) radiated to field point at (a),(b),(c) 4.5 kHz and (d),(e),(f) 7.0 kHz for 4 × 4 tessellated array with $\gamma = 55°$. In (a),(d) the fold angle is $\theta = 20°$, in (b),(e) $\theta = 40°$, in (c),(f) $\theta = 60°$. The inset schematics illustrate the folding of this array. Solid curves are BEM results; dashed curves are analytical predictions.

arrays are an important focus of the authors' continuing research.

Figure 4 shows the SPL as determined through the theoretical and BEM modeling approaches for the 4 × 4 array with an edge angle $\gamma = 85°$. This array considerably changes shape over the course of folding from $\theta = 20$ to 40, and then to 60°, as seen in the Fig. 4 insets. The layout and line styles are identical to the presentation methods of Fig. 3. The comparison of results reveals that folding the array can significantly modulate the depth of a pressure node—Figs. 4(a) and 4(b) at 4.5 kHz with $\phi = \pi/4$ and $\phi = 3\pi/4$ rad—which more greatly isolates the beam of sound reaching broadside. A similar large influence on the angular location of sidelobes is induced by folding such as comparing the changes at $\phi = \pi/2$ rad between Figs. 4(a) and 4(b) at 4.5 kHz or Figs. 4(d) and 4(e) at 7.0 kHz. These trends, as well as quantitative values of angular position and SPL, are clearly shared by the BEM and analytical model results. Yet, the analysis is less useful in predicting the acoustic energy distribution across a wide range of space when the fold angle is large, such as $\theta = 60°$, once again showing a deficiency in the overall SPL prediction for this considerable extent of folding. Nevertheless, as Figs. 4(c) and 4(f) show [as well as Figs. 3(c) and 3(f)], the analysis is still able to accurately reconstruct the location of sidelobes and their relative SPL difference to broadside. In another relevant comparison, for the results of Figs. 3 and 4 the BEM model requires 220 s (multi-core processing) to compute while the analysis is complete after 9 ms (single-core processing). As a tool for expedient preliminary design guidance girded with theoretical underpinnings, the more than 24 000 times reduction in

computation time provided by the analytical formulation is a strong case in favor of its utilization for beamfolding prediction, despite imperfections.

C. Unit cell beam pattern prediction evaluation

Continued utilization of the theoretical model and subsequent comparison to BEM results yields comparable conclusions to those reported in Sec. III B. But observing critically, such predictive performance is not necessarily an assessment of the altered assumptions employed in the analytical formulation from the conventional solution approach to Rayleigh's integral. Considering Eq. (9), the field point pressure is dependent upon the product of two beam patterns, one for the array h and one that is the sum of contributions from the cells $h_{cell,i}$. Figure 5 plots a comparison of the beam pattern amplitudes; the cell beam pattern is broken into its components and normalized by their respective areas. The results are generated considering the 4 × 4 tessellated array with $\gamma = 55°$, $\beta = 45°$, and $\phi = -5\pi/6$ rad at fold angles θ of (a) 20° and (b) 60°. Numerous, important factors are apparent in Fig. 5. First, because these beam patterns are multiplied together toward yielding the total SPL at the field point, the array beam pattern will clearly dominate the far field sound propagation at lower frequencies because of the zeros (or very small beam pattern amplitudes in dB). This is intuitive within the scope of array processing because one cannot appreciably beam sound using a transducer that has a characteristic length small with respect to the wavelength. Here, the characteristic length is the long diagonal of the transducer facets, around 39 mm, which corresponds to an acoustic wavelength associated with frequency
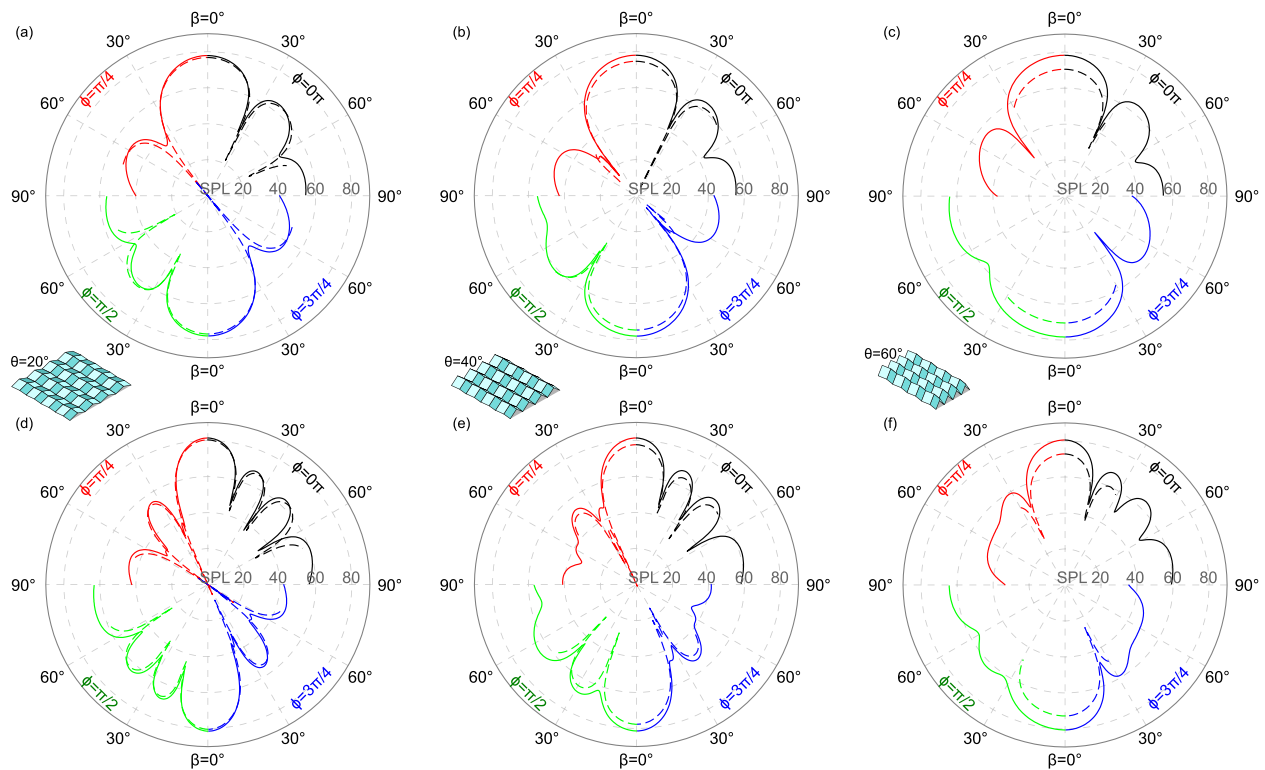
J. Acoust. Soc. Am. **141** (1), January 2017

Danielle T. Lynd and Ryan L. Harne 485

FIG. 4. (Color online) SPL (dB re 20 μPa) radiated to field point at (a),(b),(c) 4.5 kHz and (d),(e),(f) 7.0 kHz for 4 × 4 tessellated array with $\gamma = 85°$. In (a),(d) the fold angle is $\theta = 20°$, in (b),(e) $\theta = 40°$, in (c),(f) $\theta = 60°$. The inset schematics illustrate the folding of this array. Solid curves are BEM results; dashed curves are analytical predictions.

around 8.79 kHz. A significant means to guide sound in space with the transducer itself would require operating the array around twice this frequency or greater. Thus, the array, which has a much larger characteristic length, around 239 mm, by its assembly of distributed transducers, is the origin for directional energy delivery in the low frequency region. It is seen that folding the arraying from θ of (a) 20° to (b) 60° greatly shifts the spectral placement of the nodes, giving rise to the principal acoustic beamfolding influence in this case.

Yet, these observations do not draw a conclusion as to the model efficacy at its core, namely, with respect to the conventional assumptions that are altered in its formulation. To put the model to test in a frequency range where Fig. 5 suggests that the beam pattern of the unit cell itself will exhibit directionality, Fig. 6 plots the SPL at the field point at 7.0 and 15 kHz, top and bottom rows, respectively, for the single unit cell with $\gamma = 55°$. To better ensure that the BEM results are accurate at 15 kHz, the mesh is refined further such that there are 9.4 elements per wavelength. Carefully examining the comparison between the computational and analytical results in Fig. 6, it is clear that the theoretical approach has little difficulty reconstructing the SPL at 7 kHz (top row) using BEM model output as the correct benchmark, although, again the theoretical approach underpredicts the overall SPL for the higher fold angle $\theta = 60°$. At this frequency, the ratio of wavelength to characteristic length of the facets (the long diagonal) is approximately 5:4, and the BEM model effectively accounts for the longer wavelength diffraction and reflection phenomena that the analysis neglects in its strict consideration of line-of-sight waves.

Interestingly, at 15 kHz (Fig. 6, bottom row) the analysis provides more accurate predictions than at the lower frequency: the discrepancy of overall SPL at all fold angles is considerably reduced. Here, the ratio of wavelength to characteristic length is approximately 23:40, and the BEM results
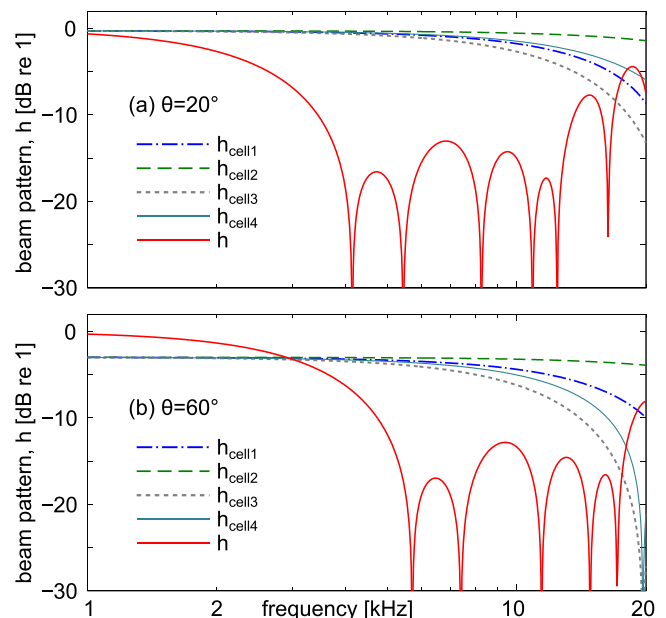

FIG. 5. (Color online) Amplitude of beam patterns of the individual unit cell parallelogram transducers $h_{\text{cell},i}$, $i = 1, 2, 3, 4$, and of the array h for the 4 × 4 tessellated array with $\gamma = 55°$, $\beta = 45°$, and $\phi = -5\pi/6$ rad at fold angles θ of (a) 20° and (b) 60°.

Danielle T. Lynd and Ryan L. Harne

and analytical results show signs of node and sidelobe formation as a result of the similarity of acoustic-to-structural dimensions. Based on this ratio and given the structural configuration involved, it is possible that high frequency diffraction phenomena (i.e., blocking) occur, which would explain the reduction in SPL levels shown in the BEM results and similarly accounted for in the analysis. These results suggest that the unit cell beam patterns, which provide only amplitude reductions at lower frequencies and high fold angles [see Fig. 5(b)] may contribute too greatly in predictions of SPL at lower frequencies by virtue of neglecting the passage of waves via the weak low frequency diffraction. In contrast, the analytical assumption that only line-of-sight waves contribute to far field point is genuinely borne out at higher frequencies where the BEM model results agree that blocking effects non-trivially participate to the far field sound levels.

After scrutinizing Figs. 5 and 6, the careful reader is likely to raise the following question: if the cell beam pattern does not greatly contribute to the overall directionality in some frequency ranges, can it be neglected with the predictions instead being solely based on variation in the array beam pattern? The answer to such a question is provided by examples in Fig. 7. The top row presents the field point SPL at 7.0 kHz delivered from a 4×4 tessellated array using $\gamma = 85°$ with fold angles (a) $\theta = 2°$ (almost unfolded) and (b) $\theta = 40°$. The bottom row presents SPL at 15 kHz where $\gamma = 55°$ with fold angles θ (a) $2°$ and (b) $40°$. The solid curves denote the BEM model results, the dashed curves denote the full analytical model results, while the dotted curves are predictions from the analytical model considering only the array

beam pattern (i.e., cell beam patterns are set to unit values to generate the dotted curves results).

At 7.0 kHz with $\gamma = 85°$, the ratio of wavelength to characteristic length is approximately 3:2, and Fig. 7(a) shows that the array beam pattern is sufficient to accurately predict the directionality of sound radiation at least within about $\beta = \pm 30°$. On the other hand, the salient sidelobe and node features beyond this angular space are less effectively reconstructed by the analysis if it only employs information from the array beam pattern. Once folded to $\theta = 40°$, Fig. 7(b), the discrepancies are reduced, particularly because the full analytical computation struggles in reconstructing the overall SPL as accurately. Nevertheless, while the full analytical prediction still reproduces the sidelobe locations and relative SPL differences between sidelobes and the major lobe for the higher fold angle $\theta = 40°$, the analysis using only the array beam pattern cannot perform this essential function since sidelobe levels are clearly skewed from BEM results.

At 15 kHz with $\gamma = 55°$, the ratio of wavelength to characteristic length is approximately 23:40, and the bottom row results of Fig. 7 reveal that neglecting the cell beam pattern where it is influential in determining the total directionality has adverse effects. For instance, outside of the narrow major lobe $\beta = \pm 5°$, using only the array beam pattern leads to severe discrepancies between the analytical predictions and BEM results with errors up to about 40 dB, e.g., Fig. 7(c) for $\theta = 2°$ and $\phi = \pi/2$ where a second "major lobe" is predicted for an end-fire ($\beta = 90°$) configuration by the analytical approach using only the array beam pattern. In contrast, by deploying the full analytical model with the explicit
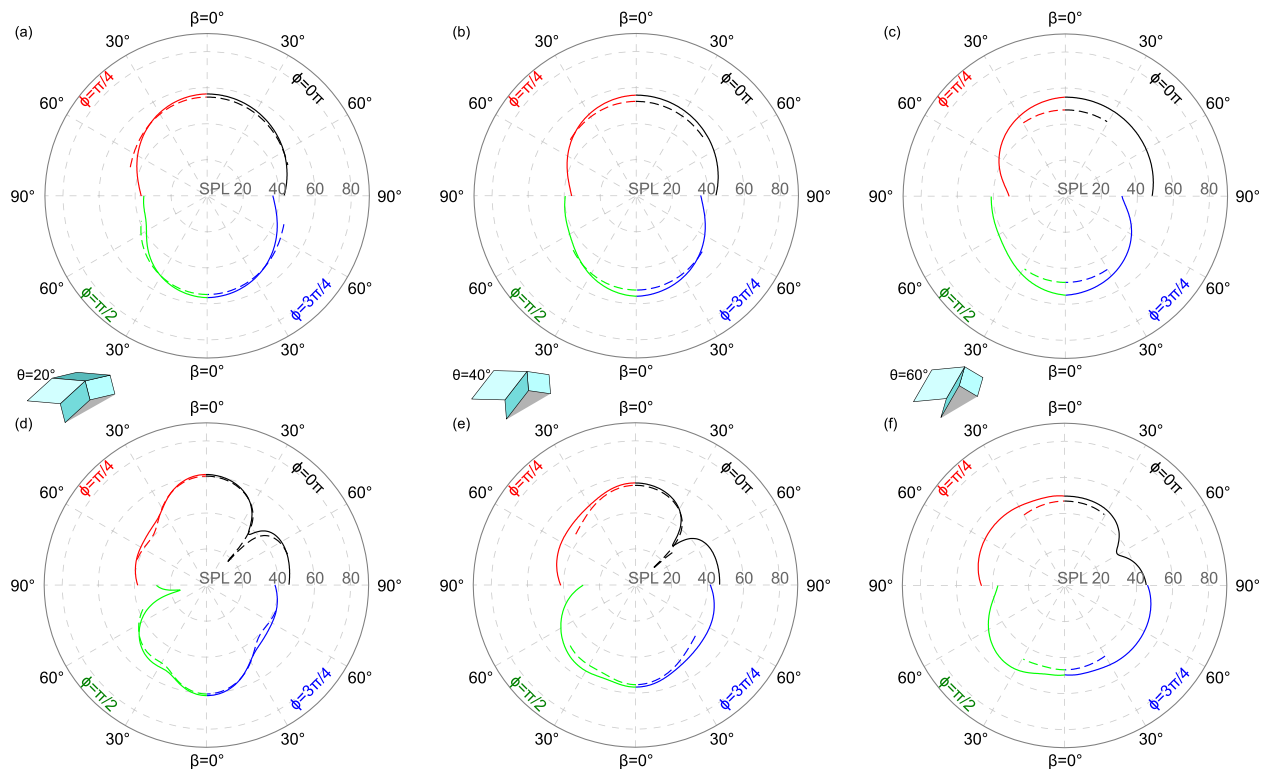

FIG. 6. (Color online) SPL (dB re 20 μPa) radiated to field point at (a),(b),(c) 7.0 kHz and (d),(e),(f) 15 kHz for the tessellated unit cell with $\gamma = 55°$. In (a),(d) the fold angle is $\theta = 20°$, in (b),(e) $\theta = 40°$, in (c),(f) $\theta = 60°$. The inset schematics illustrate the folding of the unit cell. Solid curves are BEM results; dashed curves are analytical predictions.
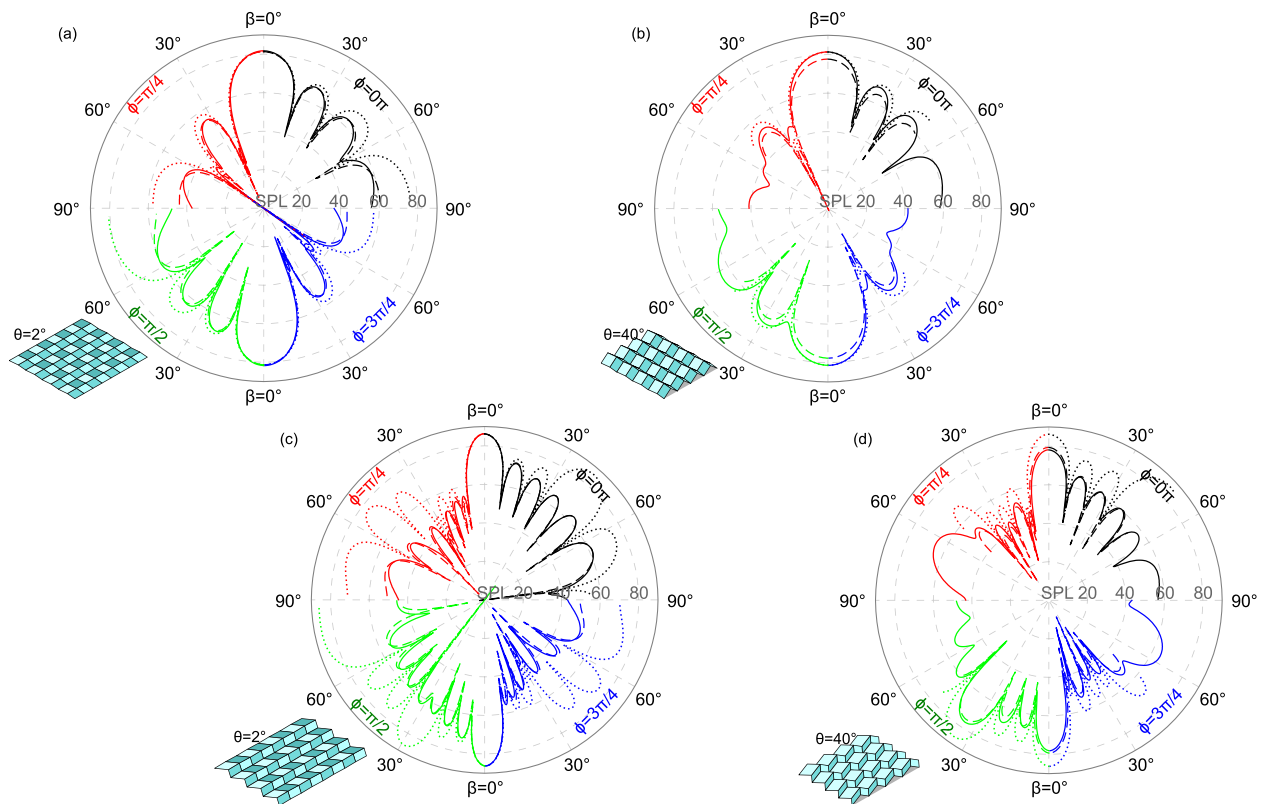
FIG. 7. (Color online) SPL (dB re 20 μPa) radiated to field point from 4 × 4 tessellated array. (Top) $\gamma = 85°$ and 7.0 kHz with θ (a) 2° and (b) 40°. (Bottom) $\gamma = 55°$ and 15 kHz with θ (c) 2° and (d) 40°. The inset schematics illustrate the array folding. Solid curves are BEM results; dashed curves are analytical predictions; dotted curves are analytical predictions using only the directional response associated with the array beam pattern.

accounting for transducer folding and planar variation of cell beam pattern, which are critical model formulation nuances absent in Ref. 30 but established here, the theoretical approach (dashed curves) regains its utility to accurately reconstruct the sound energy-guiding capability of the folding, tessellated array. As shown for both the mostly unfolded $\theta = 2°$ and folded $\theta = 40°$ configurations in Figs. 7(c) and 7(d), respectively, the full analytical method provides results that are almost identical to the BEM simulations over the elevation angle range where its predictions are viable. The results give plain evidence that the complete analytical model formulation, based on a classical approximate solution to Rayleigh's integral, is remarkably accurate, despite its underlying altered assumptions. For completeness, using the refined mesh at 15 kHz, the computation time by BEM is 991 s to generate one of the plotsin Figs. 7(c) or 7(d), while the full analysis requires 7 ms to compute: more than five orders of magnitude difference in processing time.

IV. CONCLUSIONS

Acoustic beamfolding represents a powerful concept to simply and significantly guide sound energy, and wave reception sensitivity by virtue of reciprocity. Yet, a robust modeling approach is required to maximize the concept potential, lest time-consuming simulation-based methods be fully relied upon for design and deployment guidance. This research carefully investigated and considerably enhanced an analytical model based on approximate solutions to Rayleigh's integral to efficiently determine the sound energy delivered to a field point in consequence to a foldable, tessellated array of harmonically driven acoustic transducers. Despite altering conventional assumptions regarding the Rayleigh's integral formulation and approximate solution, through a deep scrutiny of the analytical results with respect to high fidelity BEM simulations, this research concludes that the predictive capability of the analytical approach strongly merits its implementation to characterize energy-guiding performance of foldable arrays built on tessellated architectures. Future utilization of this modeling approach will include leveraging it, via inverse spatial Fourier transforms, to identify tessellation topologies and folding extents that promote a required directionality of wave propagation, while ongoing experimental efforts seek to illuminate practical factors involved in fabricating and deploying foldable, tessellated arrays.

Danielle T. Lynd and Ryan L. Harne

[1]C. H. Sherman and J. L. Butler, *Transducers and Arrays for Underwater Sound* (Springer, New York, 2007).

[2]D. H. Turnbull and F. S. Foster, "Beam steering with pulsed two-dimensional transducer arrays," IEEE Trans. Ultrason. Ferroelectr. Freq. Control **38**, 320–333 (1991).

[3]"Product Sheet: LRAD 100X" (LRAD Corporation, San Diego, CA, 2015).

[4]C. E. Graber, "Robotic sentry with low dispersion acoustic projector," U.S. patent 8,248,473,2012 (August 21, 2012).

[5]F. M. Fazi, "Sound field reproduction," Ph.D. dissertation, Institute of Sound and Vibration Research, University of Southampton, Southampton, UK, 2010.

[6]W. A. Veronesi and J. D. Mayndard, "Digital holographic reconstruction of sources with arbitrarily shaped surfaces," J. Acoust. Soc. Am. **85**, 588–598 (1989).

[7]J. D. Maynard, E. G. Williams, and Y. Lee, "Nearfield acoustic holography: I. Theory of generalized holography and the development of NAH," J. Acoust. Soc. Am. **78**, 1395–1413 (1985).

[8]J. Benesty, J. Chen, and Y. Huang, *Microphone Array Signal Processing* (Springer, Berlin, 2008).

[9]Y. T. Cho and M. J. Roan, "Adaptive near-field beamforming techniques for sound source imaging," J. Acoust. Soc. Am. **125**, 944–957 (2009).

[10]L. C. Parra, "Steerable frequency-invariant beamforming arbitrary arrays," J. Acoust. Soc. Am. **119**, 3839–3847 (2006).

[11]J. G. Ryan and R. A. Goubran, "Array optimization applied in the near field of a microphone array," IEEE Trans. Speech Audio Process. **8**, 173–176 (2000).

[12]D. H. Johnson and D. E. Dudgeon, *Array Signal Processing: Concepts and Techniques* (Prentice-Hall, Englewood Cliffs, NJ, 1993).

[13]J. Benesty and J. Chen, *Study and Design of Differential Microphone Arrays* (Springer, Berlin, 2013).

[14]D. W. E. Schobben, *Real-time Adaptive Concepts in Acoustics: Blind Signal Separation and Multichannel Echo Cancellation* (Springer, Dordrecht, 2001).

[15]J. A. Jensen, H. Holten-Lund, R. T. Nilsson, M. Hansen, U. D. Larsen, R. P. Domsten, B. G. Tomov, M. B. Stuart, S. I. Nikolov, M. J. Pihl, Y. Du, J. H. Rasmussen, and M. F. Rasmussen, "SARUS: A synthetic aperture real-time ultrasound system," IEEE Trans. Ultrason. Ferroelectr. Freq. Control **60**, 1838–1852 (2013).

[16]X. Liu, S. Yao, S. V. Georgakopoulos, B. S. Cook, and M. M. Tentzeris, "Reconfigurable helical antenna based on an origami structure for wireless communication system," in *Proceedings of the 2014 IEEE MTT-S International Microwave Symposium* (2014), pp. 1–4.

[17]S. Bildik, S. Dieter, C. Fritzsch, W. Menzel, and R. Jakoby, "Reconfigurable folded recflectarray antenna based upon liquid crystal technology," IEEE Trans. Antennas Propag. **63**, 122–132 (2015).

[18]K. Fuchi, A. R. Diaz, E. J. Rothwell, R. O. Ouedraogo, and J. Tang, "An origami tunable metamaterial," J. Appl. Phys. **111**, 084905 (2012).

[19]K. Fuchi, P. R. Buskohl, G. Bazzan, M. F. Durstock, J. J. Joo, G. W. Reich, and R. A. Vaia, "Spatial tuning of a RF frequency selective surface through origami," Proc. SPIE **9844**, 98440W (2016).

[20]The Karl G. Jansky Very Large Array, [available at https://science.nrao.edu/facilities/vla/ (Last viewed April 17, 2016).

[21]P. Wang-Iverson, R. J. Lang, and M. Yim, eds., *Origami 5: Fifth International Meeting of Origami Science, Mathematics, and Education* (CRC Press, Boca Raton, FL, 2011).

[22]R. J. Lang, ed., *Origami 4* (Peters, Natick, MA, 2009).

[23]C. D. Onal, M. T. Tolley, R. J. Wood, and D. Rus, "Origami-inspired printed robots," IEEE/ASME Trans. Mechatron. **20**, 2214–2221 (2015).

[24]E. A. Peraza-Hernandez, D. J. Hartl, R. J. Malak, Jr., and D. C. Lagoudas, "Origami-inspired active structures: A synthesis and review," Smart Mater. Struct. **23**, 094001 (2014).

[25]K. Wang and Y. Chen, "Folding a patterned cylinder by rigid origami," in *Origami 5: Fifth International Meeting of Origami Science, Mathematics, and Education*, edited by P. Wang-Iverson, R. J. Lang, and M. Yim (CRC Press, Boca Raton, FL, 2011), pp. 265–276.

[26]M. Schenk and S. D. Guest, "Geometry of Miura-folded metamaterials," Proc. Natl. Acad. Sci. U.S.A. **110**, 3276–3281 (2013).

[27]J. T. B. Overvelde, T. A. de Jong, Y. Shevchenko, S. A. Becerra, G. M. Whitesides, J. C. Weaver, C. Hoberman, and K. Bertoldi, "A three-dimensional actuated origami-inspired transformable metamaterial with multiple degrees of freedom," Nat. Commun. **7**, 10929 (2016).

[28]S. A. Zirbel, R. J. Lang, M. W. Thomson, D. A. Sigel, P. E. Walkemeyer, B. P. Trease, S. P. Magleby, and L. L. Howell, "Accommodating thickness in origami-based deployable arrays," J. Mech. Des. **135**, 111005 (2013).

[29]M. Schenk and S. D. Guest, "Origami folding: A structural engineering approach," in *Origami 5: Fifth International Meeting of Origami Science, Mathematics, and Education*, edited by P. Wang-Iverson, R. J. Lang, and M. Yim (CRC Press, Boca Raton, FL, 2011), pp. 291–304.

[30]R. L. Harne and D. T. Lynd, "Origami acoustics: Using principles of folding structural acoustics for simple and large focusing of sound energy," Smart Mater. Struct. **25**, 085031 (2016).

[31]K. Miura, "Method of packaging and deployment of large membranes in space," Report No. 618, The Institute of Space and Astronautical Science (1985).

[32]S. Liu, G. Lu, Y. Chen, and Y. W. Leong, "Deformation of the Miura-ori patterned sheet," Int. J. Mech. Sci. **99**, 130–142 (2015).

[33]J. W. Strutt, *The Theory of Sound* (MacMillian, London, 1894).

[34]S. A. Hambric, S. H. Sung, and D. J. Nefske, *Engineering Vibroacoustic Analysis: Methods and Applications* (Wiley, Chichester, 2016).

[35]M. Postema, *Fundamentals of Medical Ultrasonics* (Spon, New York, 2011).

[36]D. T. Blackstock, *Fundamentals of Physical Acoustics* (Wiley, New York, 2000).

[37]V. C. Henriquez and P. M. Juhl, "OpenBEM—An open source boundary element method software in acoustics," in *Proceedings of Internoise 2010*, Lison, Portugal (2010), pp. 1–10.

[38]This contrasts with rotating or translating a beam-steered array, like classical antenna scanning in RADAR systems, which is occasionally also referred to as mechanical signal processing.

J. Acoust. Soc. Am. **141** (1), January 2017

Danielle T. Lynd and Ryan L. Harne   489